

Showcasing research from Professor Jeongsuk Seo's laboratory, Department of Chemistry, College of Natural Sciences, Chonnam National University, Gwangju, Republic of Korea.

A N-doped  $\text{NbO}_x$  nanoparticle electrocatalyst deposited on carbon black for oxygen reduction and evolution reactions in alkaline media

There is a growing interest in the novel bifunctional electrocatalyst for oxygen reduction (ORR) and evolution reactions (OER), for application in electrochemical energy conversion systems. N-doped  $\text{NbO}_x$ /CB nanoparticles of approximately 3 nm in size, for the first time, are introduced as an active and stable bifunctional oxygen electrocatalyst in alkaline media. The nanosize control and modified surface of the  $\text{NbO}_x$  catalyst composed of multivalence, originating from the synthesis route including potentiostatic electrodeposition in a nonaqueous solution and subsequent annealing in a  $\text{NH}_3$  flow, largely promote the oxygen electrocatalyses.

### As featured in:



See Jeongsuk Seo *et al.*,  
*Mater. Adv.*, 2022, **3**, 5315.



Cite this: *Mater. Adv.*, 2022, 3, 5315

## A N-doped $\text{NbO}_x$ nanoparticle electrocatalyst deposited on carbon black for oxygen reduction and evolution reactions in alkaline media†

Jeongsuk Seo, <sup>a</sup> Won-Jin Moon, <sup>b</sup> Wan-Gil Jung <sup>b</sup> and Jun-Woo Park <sup>c</sup>

There is growing interest in novel bifunctional electrocatalysts for oxygen reduction (ORR) and evolution reactions (OER), for application in electrochemical energy conversion systems. While ultrafine oxides have been reported as efficient electrocatalysts for the ORR and OER, there are no reports on ultrafine oxides based on the group 4 or 5 metals as a bifunctional oxygen electrocatalyst. Herein, we present and demonstrate N-doped  $\text{NbO}_x$ /CB nanoparticles as a highly active and stable, bifunctional oxygen electrocatalyst in alkaline media. The  $\text{NbO}_x$  nanoparticles approximately 3 nm in size were successfully synthesized on carbon black (CB) by potentiostatic electrodeposition. The employment of a CB support with a large surface area resulted in a loading amount of 20 wt% Nb in the N-doped  $\text{NbO}_x$ /CB and a uniform distribution of the oxide on CB, leading to an increase of the reaction site. The subsequent annealing in an  $\text{NH}_3$  flow decreased the concentration of oxygen and intercalated a small amount of nitrogen in the as-deposited  $\text{NbO}_x$  particles, largely lowering the overpotentials of the ORR and OER. The surface Nb species on the N-doped  $\text{NbO}_x$  particles were made of multivalent  $\text{Nb}^{4+}$  and  $\text{Nb}^{5+}$ . As a result, the prepared N-doped  $\text{NbO}_x$ /CB nanoparticles exhibited high catalytic activities for both the ORR and OER in a 0.1 M KOH solution. The potential difference,  $\Delta E$ , indicating an index for the bifunctional oxygen electrocatalyst, was 1.13 V, which was comparable to those of the commercial 20 wt% Pt/CB and Ir/CB. In addition, the current densities obtained for the nanoparticles were significantly steady for both the long-term ORR and OER in alkaline media. Together these results demonstrate the N-doped  $\text{NbO}_x$ /CB nanoparticles as potential bifunctional oxygen electrocatalysts.

Received 14th March 2022,  
Accepted 9th May 2022

DOI: 10.1039/d2ma00292b

rsc.li/materials-advances

## 1. Introduction

Novel electrocatalysts for the oxygen reduction reaction (ORR) and oxygen evolution reaction (OER) have attracted significant research interest for their application in various energy conversion and storage systems such as regenerative fuel cells, water electrolysis, and metal-air batteries.<sup>1–3</sup> In addition, the environmental regulations due to global climate change, the depletion of fossil fuels, and increasing energy consumption, have accelerated the exploration of oxygen electrocatalysts that boost the efficiency of the four-electron pathway to drive the ORR or OER. An ideal

electrocatalyst should be made of materials that can withstand the conditions of the energy systems, *e.g.*, a high or low pH level and a wide potential window, for efficient and long-term performance. With this background, many potential candidates including metal oxides and carbon materials have been proposed as promising ORR and OER electrocatalysts.<sup>1–6</sup>

In particular, bi-functional oxygen electrocatalysts have attracted much attention because they enable cost reduction and simplification of energy systems, and also allow metal-air batteries to operate charge–discharge cycles.<sup>2,4,5,7</sup>  $\text{RuO}_2$  and  $\text{IrO}_2$  electrocatalysts have been shown to be very active for the OER in acidic and alkaline electrolytes,<sup>8</sup> while Pt nanoparticles supported on carbon, as a commercial fuel cell electrocatalyst, have shown high performance for the ORR in acidic media.<sup>1</sup> However, the typical oxygen electrocatalysts are all rare metals leading to an increase in production cost, and have limited activity for the counter oxygen reaction. Initiating from manganese oxide  $\text{MnO}_2$ ,<sup>9,10</sup> transition metal oxides with special crystal structures, such as spinel oxides with a formula of  $\text{AB}_2\text{O}_4$  (A = divalent metal ion; B = trivalent metal ion) or perovskite oxides with a formula of  $\text{ABO}_3$  (A = alkaline-earth metal ion;

<sup>a</sup> Department of Chemistry, College of Natural Sciences, Chonnam National University, 77 Yongbong-ro, Buk-gu, Gwangju 61186, Republic of Korea.  
E-mail: [j\\_seo@chonnam.ac.kr](mailto:j_seo@chonnam.ac.kr)

<sup>b</sup> Korea Basic Science Institute, Gwangju Center, 77 Yongbong-ro, Buk-gu, Gwangju 61186, Republic of Korea

<sup>c</sup> Next-Generation Battery Research Center, Korea Electrotechnology Research Institute, 12 Bulmosan-ro 10beon-gil, Seongsan-gu, Changwon-si, Gyeongsangnam-do 51543, Republic of Korea

† Electronic supplementary information (ESI) available. See DOI: <https://doi.org/10.1039/d2ma00292b>



$B =$  transition metal ion), were found to be active for both the ORR and OER in alkaline media.<sup>2,4,5,11,12</sup> The crystal structures allow the transition metals to be tuned to variable valences separately and activated for each reaction. It therefore causes the oxygen redox electrochemistry of single catalysts.

Cobalt oxide  $\text{Co}_3\text{O}_4$  in a spinel structure has two different valences of  $\text{Co}^{2+}$  and  $\text{Co}^{3+}$  ions, and  $\text{Co}^{3+}$  is known to act as a donor-accepter reduction site for the ORR.<sup>13,14</sup> In this case, the electron transfer between the cations with different valences requires low activation energy. In a previous study on  $\text{Mn}_x\text{Co}_{3-x}\text{O}_4$ , the ORR activity was enhanced by increasing the amount of  $\text{Mn}^{4+}/\text{Mn}^{3+}$  redox pairs, and the surface  $\text{Co}^{3+}$  was regarded as an active site for the OER.<sup>15</sup> In perovskite oxides described by the formula  $\text{A}_{1-x}\text{A}'_x\text{B}_{1-y}\text{B}'_y\text{O}_3$ , the substitution of the A-site by another element influenced the ability to adsorb oxygen, while that of the B-site affected the activity of the adsorbed oxygen during the ORR.<sup>16,17</sup>  $\text{La}_{0.6}\text{Ca}_{0.4}\text{CoO}_3$  exhibited improved ORR and OER catalytic activities simultaneously, and its electrocatalytic properties were enhanced by tuning the oxidation state of Co species.<sup>18,19</sup> It was also revealed that the higher oxidation state of the surface Co species enhanced the oxygen electrocatalysis.<sup>20</sup> These results indicate that the different valences of metals that co-existed on a single catalyst were a requirement to be a bi-functional oxygen electrocatalyst.

Group 4 and 5 transition metals such as Ti, Nb, and Ta are known to have multi-valence, and several Ti-, Nb-, and Ta-based compounds have been reported as ORR electrocatalysts in acidic and alkaline solutions.<sup>21-26</sup> Although nitrides, carbides, and mixed compounds were tested for boosting ORR electrocatalytic activities by doping with additional elements and by applying heat treatments, their short-term stability in acidic electrolytes was an obstacle for polymer electrolyte fuel cell applications. In addition, it was rarely reported that Ta-based catalysts deposited on carbon black (CB) with a predominant crystal phase  $\text{Na}_2\text{Ta}_8\text{O}_{21}$ , prepared by a microemulsion method, were activated as bi-functional oxygen electrocatalysts in 0.1 M NaOH aqueous solution.<sup>27</sup> The electrocatalytic activities using the Ta-based oxides were unsatisfactory, even the anodic current for the OER did not reach  $10 \text{ mA cm}^{-2}$  at potentials lower than  $2.0 \text{ V}_{\text{RHE}}$ . The metal oxides with a maximum valence, *e.g.*,  $\text{Ta}_2\text{O}_5$  and  $\text{Nb}_2\text{O}_5$ , were chemically the most stable under acidic and alkaline conditions.<sup>22,23,27,28</sup> Nevertheless, these oxides are insulators in bulk, thus resulting in low electrocatalytic activity. The nanosize control of  $\text{NbO}_x$ ,  $\text{ZrO}_x$ , and  $\text{TaO}_x$  particles in  $1 \sim 2 \text{ nm}$  diameter dispersed on CB was very effective in improving electrocatalytic activity for ORR in acid media.<sup>24,25,28</sup> The transition metals in the oxide nanoparticles were composed of two or three different oxidation states according to XPS analyses. The ultrafine  $\text{TaO}_x/\text{CB}$  electrocatalysts activated the ORR in a 0.1 M  $\text{H}_2\text{SO}_4$  electrolyte *via* nearly a four-electron transfer pathway and also maintained long-term stability for 10,000 cycles.<sup>28</sup> However, there are no reports on the ultrafine oxides based on the group 4 or 5 metals as bifunctional oxygen electrocatalysts in alkaline media.

Herein, for the first time, we present N-doped  $\text{NbO}_x$  nanoparticles highly dispersed on CB (designated as N-doped

$\text{NbO}_x/\text{CB}$  hereafter) as an active bifunctional oxygen electrocatalyst in alkaline media. The oxide nanoparticles that were approximately 3 nm were successfully synthesized at CB surfaces by electrodeposition in a nonaqueous Nb-based solution followed by annealing treatment in a  $\text{NH}_3$  flow. The N-doped  $\text{NbO}_x$  particles were composed of  $\text{Nb}^{4+}$  and  $\text{Nb}^{5+}$  species. The employment of a CB support with a large surface area of  $1251 \text{ m}^2 \text{ g}^{-1}$  significantly increased the loading amount of  $\text{NbO}_x$  particles, and therefore augmented the reaction sites for the oxygen reactions. These physical and surface properties resulted in high activities in both the ORR and OER over the N-doped  $\text{NbO}_x/\text{CB}$  particles in a 0.1 M KOH solution. In particular, the annealing in the  $\text{NH}_3$  flow significantly lowered the overpotentials for the ORR and OER due to a decrease in the concentration of oxygen and additional doping of nitrogen in the  $\text{NbO}_x$  catalyst leading to decreased charge transfer resistance. Also, the current densities over the nanoparticles were stable for both long-term ORR and OER. These results demonstrated that the N-doped  $\text{NbO}_x/\text{CB}$  nanoparticles were active bifunctional oxygen electrocatalysts in alkaline media.

## 2. Experimental section

### 2.1. Preparation of N-doped $\text{NbO}_x/\text{CB}$ powder catalysts

The  $\text{NbO}_x$  species were loaded on the CB powder surfaces through potentiostatic electrodeposition in a nonaqueous Nb-based solution. Ten mg of CB powder (Ketjen black EC-600JD, Akzo Nobel Functional Chemicals) was sandwiched between two carbon paper sheets (AvCarb MGL190, AvCarb Material Solutions). A home-made electrodeposition cell was used to fix the sandwiched CB assembly, presented in a previous report.<sup>28</sup> The cell as a working electrode was mounted on a typical three-electrode system using a potentiostat (CHI700E, CH Instruments, Inc.). A carbon rod and  $\text{Ag}/\text{Ag}^+$  were used as counter and reference electrodes, respectively. The nonaqueous Nb-based solution consisted of 10 mM  $\text{NbCl}_5$  (99.9%, Sigma-Aldrich), 10 mM  $\text{NH}_4\text{Cl}$  (99%, Kanto Chemical) as a supporting electrolyte, and an anhydrous ethanol solvent. In order to electrodeposit  $\text{NbO}_x$  species on the CB, a constant potential of  $-0.4 \text{ V}_{\text{Ag}/\text{Ag}^+}$  was applied to the working cell for 30 s in the stirred Ar-purged  $\text{NbCl}_5-\text{NH}_4\text{Cl}$  ethanol solution at 298 K.<sup>25</sup> The electrodeposited CB powder was washed with anhydrous ethanol to remove the remaining Nb precursor and then completely dried at 298 K. Subsequently, the resulting powder was annealed in a pure  $\text{NH}_3$  (5N grade) or Ar (5N grade) at a flow of  $200 \text{ ml min}^{-1}$  at 873 K for 1 h with a ramp rate of  $10 \text{ K min}^{-1}$ .

### 2.2. Electrochemical measurements

A catalyst slurry was prepared for ORR and OER electrochemical measurements. Two mg of the prepared N-doped  $\text{NbO}_x/\text{CB}$  powder and 12  $\mu\text{l}$  of a Nafion solution (5 wt% in water/aliphatic alcohols, Sigma-Aldrich) were dispersed in 300  $\mu\text{l}$  of isopropyl alcohol (99.9%, Kanto Chemical). The mixture was repeatedly placed in an ultrasonic bath and stirred with a magnetic stirrer to enhance the degree of dispersion. Two point five  $\mu\text{l}$  of the



catalyst slurry was dropped on a glassy carbon rotating-disk electrode (RDE; 5 mm in diameter) and dried naturally. The loading amount of catalyst was approximately  $82 \mu\text{g cm}^{-2}$ . For comparison, a commercial 20 wt% Pt/CB (Premetek Co., Pt on Vulcan XC-72) and 20 wt% Ir/CB (Premetek Co., Ir on Vulcan XC-72) catalyst slurry was also cast on the RDE in the same manner.

Electrochemical measurements were done using the RDE system, composed of Hg/HgO reference and carbon rod counter electrodes at 298 K. Cyclic and linear sweep voltammograms (CVs and LSVs) were scanned in the potential range of 2.0 to 0.10  $V_{\text{RHE}}$  at a scan rate of  $10 \text{ mV s}^{-1}$  in an Ar- or  $\text{O}_2$ -saturated 0.1 M aqueous KOH solution. The potential scale referenced by the Hg/HgO electrode was calibrated to a reversible hydrogen electrode (RHE). For rotating ring-disk electrode (RRDE) measurements, the glassy carbon disk electrode (4.0 mm in diameter) was scanned at a sweep rate of  $5 \text{ mV s}^{-1}$ , and a potential of  $1.2 \text{ V}_{\text{RHE}}$  was applied at a Pt ring electrode (5.0 mm in inner diameter; 7.0 mm in outer diameter). The  $\text{H}_2\text{O}_2$  yield detected at the ring electrode was estimated using the equation,

$$\% \text{H}_2\text{O}_2 = \frac{2i_{\text{ring}}/N}{-i_{\text{disk}} + i_{\text{ring}}/N} \times 100 \quad (1)$$

where  $i_{\text{disk}}$  and  $i_{\text{ring}}$  are the disk and ring current, respectively, and  $N$  is the current collection efficiency of the RRDE.  $N$  was determined to be 0.420 by a reduction of  $\text{K}_3[\text{Fe}(\text{CN})_6]$ . Electrochemical impedance spectroscopy (EIS; METEK Inc., Versastat3-200) of the prepared catalysts was performed at an applied potential of  $0.72 \text{ V}_{\text{RHE}}$  in the frequency range from  $10^4$  to  $10^{-1} \text{ Hz}$  with an AC amplitude of 10 mV. The acquired EIS results were fitted using a ZView program (Scribner Associates, Inc.) using an equivalent circuit model.

### 2.3. Surface and physical characterization

The crystal structure of the prepared N-doped  $\text{NbO}_x/\text{CB}$  catalysts was investigated by X-ray diffraction (XRD; MiniFlex 600, Rigaku) using  $\text{Cu K}\alpha$  radiation at 40 kV and 15 mA. The surface morphology of the N-doped  $\text{NbO}_x/\text{CB}$  nanoparticles was characterized by field emission transmission electron microscopy (FE-TEM; JEM-2200FS, JEOL). The loading amount of Nb in N-doped  $\text{NbO}_x/\text{CB}$  was determined by inductively coupled plasma optical emission spectroscopy (ICP-OES; PerkinElmer, Avio 500). The Brunauer-Emmett-Teller (BET) surface area of the prepared catalyst was determined using the BET (ASAP2020, Micromeritics Instrument Corp.) adsorption method based on the adsorption of  $\text{N}_2$  gas at 77 K. Its pore size distribution was also obtained by the Barrett-Joyner-Halenda (BJH) method using the desorption branch of the isotherm. The chemical states of Nb, O, and N species on the N-doped  $\text{NbO}_x/\text{CB}$  surface were determined by high-performance X-ray photoelectron spectroscopy (HP-XPS; K-Alpha +, Thermo Scientific), using a monochromatic X-ray source producing  $\text{Al K}\alpha$  emission with a current of 6 mA, and an acceleration voltage of 12 kV.

## 3. Results and discussion

$\text{NbO}_x$  particles were synthesized on the CB, with a large surface area, by electrodeposition at a constant potential of  $-0.4 \text{ V}_{\text{Ag}/\text{Ag}^+}$  for 30 s in 10 mM Nb-based nonaqueous solution. The resulting particles were annealed in an  $\text{NH}_3$  flow at 873 K for 1 h, so as to modify their surface properties. For comparison, it was also placed in an Ar atmosphere at the same temperature. The crystal structures of the as-deposited and annealed particles were measured by XRD analysis (Fig. S1, ESI<sup>†</sup>). The XRD pattern of the as-deposited particles showed no peaks distinguishable from that of bare CB powder. After the annealing in Ar, the XRD pattern of the particles revealed some crystallinity with a weak peak at  $26^\circ$ , nearly assignable to  $\beta\text{-NbO}_2$  (220) (ICSD #35181). In contrast, the particles annealed in  $\text{NH}_3$  did not show diffraction peaks, indicating that the particles were highly fine or amorphous. Also, the peaks for the bare CB were not shifted, presenting no introduction of nitrogen in the CB support. The surface morphology of the particles was investigated by (S)TEM measurements. The particles annealed in Ar, smaller than roughly 5 nm in size, were more discrete than the as-deposited particles, however the size of particles was largely unchanged after the annealing at 873 K (Fig. S2, ESI<sup>†</sup>). Further advanced analysis using the two samples was technically difficult because the particles were made of light elements such as oxygen and amorphous (or low crystalline). Fig. 1 exhibits STEM and TEM images of the particles annealed in  $\text{NH}_3$ . In the STEM image (Fig. 1A), the bright spots made of a relatively heavy element were well dispersed on ball-like supports. As cross-checked with the TEM image (Fig. 1B), the supports showed a typical surface morphology of Ketjen Black as CB, composed of primary particles

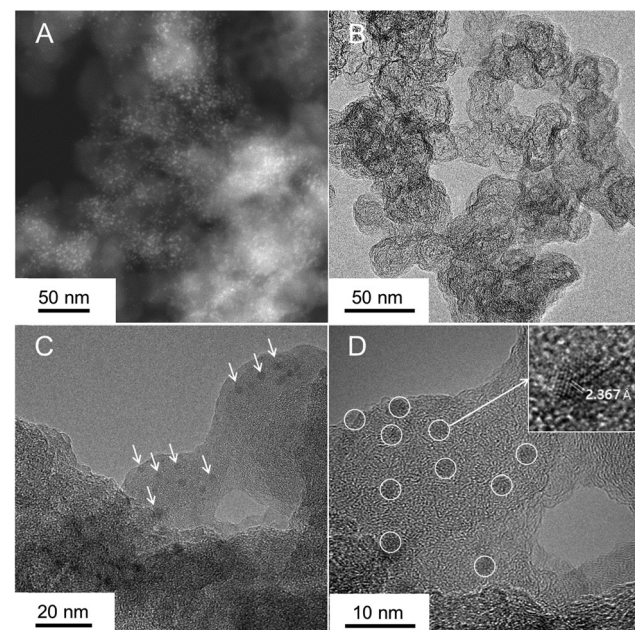


Fig. 1 (A) STEM and (B–D) TEM images of the N-doped  $\text{NbO}_x/\text{CB}$  nanoparticles, prepared by electrodeposition and subsequent annealing treatment in an  $\text{NH}_3$  flow at 873 K for 1 h.



smaller than 50 nm size.<sup>29</sup> Fine particles, approximately 3 nm size, were well-dispersed on the CB as shown in Fig. 1C and D, and were regarded as Nb-based species. The nanoparticles in the inset of Fig. 1D had lattice fringes, indicating the crystallinity of the material. Although crystalline particles were observed, their crystal structures were varied in the present stage and different from  $\beta$ -NbO<sub>2</sub> (220) observed in the XRD result (Fig. S3, ESI<sup>†</sup>). Therefore, the synthesis of catalysts by electrodeposition and subsequent annealing in NH<sub>3</sub> produced well-dispersed, crystalline Nb-based nanoparticles.

The chemical state and composition of the Nb-based species were determined by XPS analysis. Fig. 2 shows narrow-scanned Nb 3d, O 1s, and N 1s XPS spectra of the as-deposited nanoparticles and the annealed derivatives in Ar and NH<sub>3</sub> atmospheres. The Nb 3d spectra of all the samples broadened and deviated from the double splitting peaks corresponding to the fully oxidized Nb<sub>2</sub>O<sub>5</sub> (Nb<sup>5+</sup>), indicating the chemical shift to a lower valence state. Accordingly, the broad Nb 3d spectra were deconvoluted with different oxidation states of Nb<sup>5+</sup> and Nb<sup>4+</sup>.<sup>30-33</sup> The surface composition ratios of the Nb species resulting from the best-fit are summarized in Table S1 (ESI<sup>†</sup>). The convolutions clearly reveal that the electrodeposited Nb species were composed of two oxidation states indicating NbO<sub>x</sub> nanoparticles. The surface concentration of Nb<sup>5+</sup> was increased after the annealing treatment, although the presence of multivalent Nb species was still unchanged. However, according to the O 1s spectra, the concentration of oxygen species, including an OH<sup>-</sup>/H<sub>2</sub>O group adsorbed on the surface of catalyst, decreased during the annealing in Ar. The annealing of Nb-based nanoparticles in the reducing NH<sub>3</sub> accelerated the decrease in the oxygen level, while promoting the insertion of nitrogen with relatively low content. Besides the desorption of the OH<sup>-</sup>/H<sub>2</sub>O species on the surface of catalyst, the crystallization of the amorphous, as-deposited NbO<sub>x</sub> decreased the concentration of excess oxygen during the annealing at 873 K,

probably leading to the release of oxygen gas. After the annealing treatments, the decrease in the oxygen contents of catalysts caused more concentrated Nb-based particles, as proved in Fig. 1 and Fig. S2 (ESI<sup>†</sup>) showing the sizes and distributions of the annealed particles more clearly. When CB alone was annealed in NH<sub>3</sub> for comparison, the concentration of nitrogen was undetected, consistent with the XRD result (Fig. S4, ESI<sup>†</sup>). These results indicate that the nitrogen was intercalated exclusively in the NbO<sub>x</sub> nanoparticles by the nitridation process in NH<sub>3</sub> exchanging oxygen with nitrogen.<sup>34,35</sup> During the nitridation, the doped nitrogen and decreased oxygen in NbO<sub>x</sub> suppressed the crystallization of the oxide nanoparticles into single phase NbO<sub>2</sub>, consistent with the TEM result in Fig. 1D. Therefore, the prepared catalyst was identified as the NbO<sub>x</sub> nanoparticles doped with nitrogen, designated thereafter as N-doped NbO<sub>x</sub>/CB.

The amount of Nb in the catalyst, prepared by the electrodeposition at  $-0.4$  V<sub>Ag/Ag<sup>+</sup></sub> for 30 s, was determined by ICP-OES analysis. 20.1 wt% Nb was deposited on the CB surface in the electrodeposition system. In a previous report, the loading of Nb was limited to 3.6 wt% in the electrodeposition using the CP electrode mixed with Vulcan XC-72.<sup>25</sup> Therefore, the high loading amount in this study was remarkable. Moreover, the surface area of the prepared N-doped NbO<sub>x</sub>/CB and its pore size distribution were estimated by the BET adsorption method. Fig. 3(A) exhibits a N<sub>2</sub> adsorption-desorption isotherm for the N-doped NbO<sub>x</sub>/CB catalyst, which is compared with that for CB powder alone. In this study, Ketjen Black was used as the CB support for the NbO<sub>x</sub> nanoparticles because it is known as a conductive, mesoporous carbon with a large BET surface area.<sup>29</sup> The hysteresis loop for the CB was typical of the type IV adsorption isotherm according to the IUPAC classification.<sup>29,36</sup> Its pore size distribution, shown in Fig. 3(B), also exhibited the characteristic of mesoporous materials with pore diameters of 2–50 nm. The isotherm retained the mesoporous property

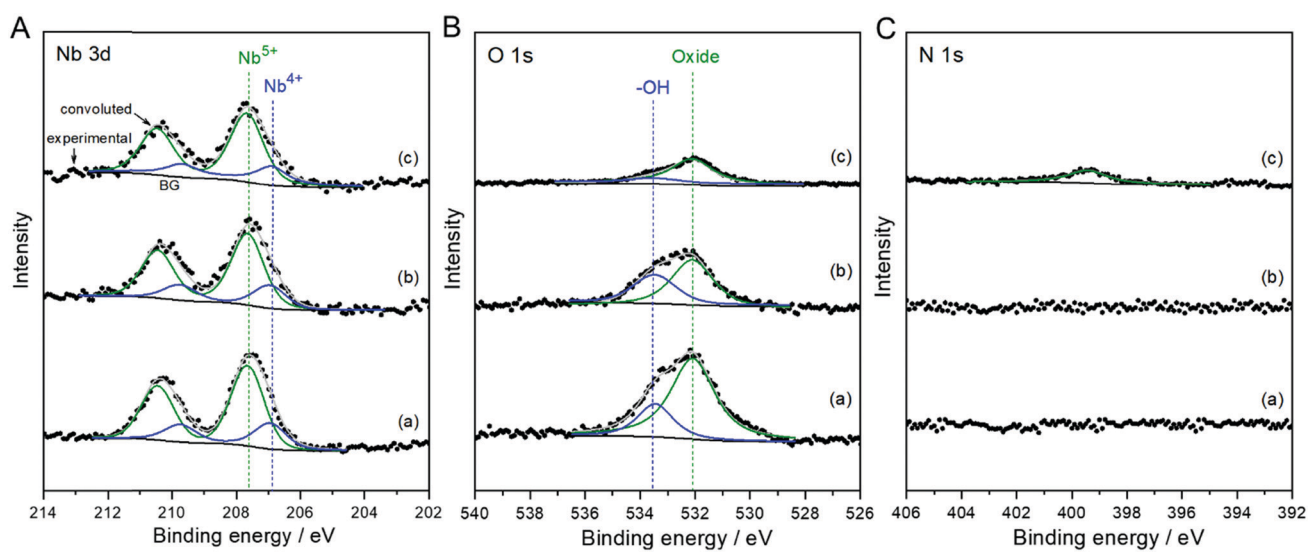


Fig. 2 Narrow-scan (A) Nb 3d, (B) O 1s, and (C) N 1s XPS spectra of NbO<sub>x</sub>/CB nanoparticles (a) as-deposited and subsequently annealed in (b) Ar and (c) NH<sub>3</sub> flows at 873 K for 1 h.



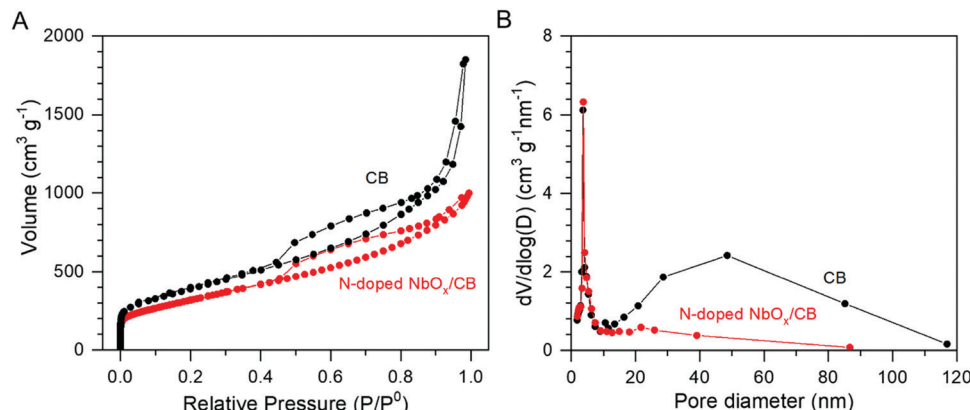


Fig. 3 (A) N<sub>2</sub> adsorption-desorption isotherms at 77 K in bare CB and N-doped NbO<sub>x</sub>/CB powder, prepared by electrodeposition and subsequent annealing treatment in NH<sub>3</sub> flow at 873 K for 1 h. (B) Pore size distribution in bare CB and N-doped NbO<sub>x</sub>/CB, deduced from N<sub>2</sub> desorption isotherms using BJH procedures.

even after the deposition of NbO<sub>x</sub> nanoparticles, although the volume trend against relative pressures became slightly lower. The BET surface areas of the N-doped NbO<sub>x</sub>/CB and CB were estimated to be 1158 and 1251 m<sup>2</sup> g<sup>-1</sup>, respectively. The coverage of NbO<sub>x</sub> particles greater than 20 wt% significantly decreased the pore volume of CB in the range of 10–50 nm, as shown in the pore size distribution. Nevertheless, the surface area of the prepared catalyst was still large because of the loading of NbO<sub>x</sub> fine particles in *ca.* 3 nm. Therefore, in this study, the application of CB with a large surface area enhanced the loading amount and uniform distribution of NbO<sub>x</sub> nanoparticles, leading to an increase in the reaction site.

Catalytic activities of the N-doped NbO<sub>x</sub>/CB nanoparticles for the ORR and OER are shown in Fig. 4(A); it exhibits CVs in Ar- and O<sub>2</sub>-purged 0.1 M KOH electrolytes with a scan rate of 10 mV s<sup>-1</sup>. The ORR was remarkably catalyzed on the nanoparticles, judged by the high cathodic current in an O<sub>2</sub> atmosphere as compared to nearly no current in an Ar atmosphere. It is clear that an O<sub>2</sub> reactant was used in the ORR. The high anodic current responsive to the OER was also observed on the

nanoparticles, regardless of the gas atmosphere. These results demonstrate that the N-doped NbO<sub>x</sub>/CB nanoparticles were active for both oxygen reactions in alkaline media. Noble metal Pt/CB, is a representative ORR electrocatalyst, while Ir/CB is a remarkable OER electrocatalyst.<sup>10</sup> For comparison, commercial 20 wt% Pt/CB and Ir/CB catalysts were estimated for the ORR and OER in O<sub>2</sub>-saturated 0.1 M KOH electrolytes and the results are shown in Fig. 4(B). The N-doped NbO<sub>x</sub>/CB nanoparticles were more active for the ORR than the Ir/CB catalyst and 140 mV less active than the Pt/CB catalyst at the half-wave potential,  $E_{1/2}$ . Also, the nanoparticles were obviously more active for the OER than Pt/CB and only 90 mV less active than Ir/CB at an anodic current density of 10 mV cm<sup>-2</sup> indicating an OER benchmark. The potential difference,  $\Delta E$ , between the ORR and OER activities for each catalyst is summarized in Table 1, showing the overall oxygen activities of the bifunctional catalysts. The potential gap for the N-doped NbO<sub>x</sub>/CB nanoparticles was 1.13 V, which was comparable to those of the noble metal catalysts. This indicates that the bifunctional activity of the nanoparticles was remarkable. Therefore, the

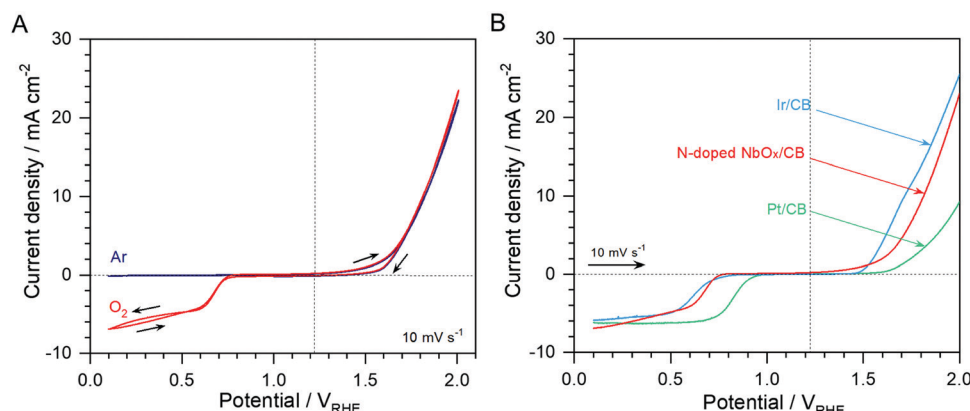


Fig. 4 (A) CVs of the N-doped NbO<sub>x</sub>/CB nanoparticles, prepared by electrodeposition and subsequent annealing treatment in a NH<sub>3</sub> flow at 873 K for 1 h. The electrochemical measurements were taken in Ar- and O<sub>2</sub>-saturated 0.1 M KOH aqueous solutions. (B) LSVs of the prepared N-doped NbO<sub>x</sub>/CB recorded by anodically sweeping the potential from 0.1 to 2.0 V<sub>RHE</sub> at a scan rate of 10 mV s<sup>-1</sup> in an O<sub>2</sub>-purged 0.1 M KOH aqueous solution. For comparison, commercial 20 wt% Pt/CB and Ir/CB powders were also measured in the same manner.



**Table 1** Bifunctional oxygen activities of N-doped  $\text{NbO}_x/\text{CB}$  electrocatalysts in 0.1 M KOH electrolytes. For comparison, commercial 20 wt% Ir/CB and Pt/CB catalysts were estimated in the same manner

Material	ORR benchmark: $E_{1/2}(\text{V})$	OER benchmark: $E(\text{V})$ at 10 mA cm $^{-2}$	Oxygen electrode $\Delta(\text{OER-ORR}): E(\text{V})$
N-doped $\text{NbO}_x/\text{CB}$	0.68 <sup>a</sup>	1.81	1.13
20 wt% Ir/CB	0.62 <sup>b</sup>	1.72	1.10
20 wt% Pt/CB	0.82 <sup>c</sup>	2.02	1.20

\* $E_{1/2}(\text{V})$  measured at  $-2.1$ <sup>(a)</sup>,  $-2.5$ <sup>(b)</sup>, and  $-3.1$  mA cm $^{-2}$ <sup>(c)</sup>.

N-doped  $\text{NbO}_x/\text{CB}$  nanoparticles, synthesized by electrodeposition and subsequent annealing, are a potential ideal reversible oxygen electrocatalyst.

To identify the nature of the bifunctional oxygen activity on the N-doped  $\text{NbO}_x/\text{CB}$  catalyst, systematic studies for the ORR and OER were carried out using the nanoparticles with different compositions. The catalytic activities of bare CB and glassy carbon were also evaluated for comparison. Fig. 5(A) shows LSVs of N-doped  $\text{NbO}_x/\text{CB}$ ,  $\text{NbO}_x/\text{CB}$  (annealed in Ar), as-deposited  $\text{NbO}_x/\text{CB}$ , CB (annealed in  $\text{NH}_3$ ), and glassy carbon for the ORR in the 0.1 M KOH solution. The current density for ORR,  $i_{\text{ORR}}$ , was calculated from the difference in cathodic current density between the  $\text{O}_2$ - and Ar-saturated atmospheres. CB, used as a support in this study, showed some activity for the ORR as compared to that of glassy carbon. It has been reported that the ORR on the CB occurred to some degree in the alkaline solution, whereas it was almost negligible in an acidic solution.<sup>28,37,38</sup> The as-deposited  $\text{NbO}_x/\text{CB}$  displayed lower activity for the ORR than CB, although its onset potential was relatively more positive. A similar result was observed in a previous report.<sup>39</sup> The lower activity was mainly ascribed to the presence of organic residues including oxygen species, remaining after the synthesis of the catalyst by the electrodeposition in a

nonaqueous electrolyte. This was also observed in the present study, as shown in the XPS spectra. However, annealing of as-deposited catalysts in different gas atmospheres remarkably enhanced the ORR activity, and the  $\text{NH}_3$  atmosphere was particularly a superior condition. The onset potential of the N-doped  $\text{NbO}_x/\text{CB}$  was 0.78 V<sub>RHE</sub> for approximately  $-0.01$  mA cm $^{-2}$ , which was significantly shifted from that of the as-deposited nanoparticles. The annealed catalysts produced higher ORR currents with more positive onset-potentials, proving that the  $\text{NbO}_x$  nanoparticles were activated as the ORR electrocatalyst. Also, it is remarkable that the increase in the loading amount of  $\text{NbO}_x$  catalyst, resulting from the employment of CB with a large surface area, produced high current density for the ORR, as compared with previous results.<sup>28,38</sup> The ORR activity of the  $\text{NbO}_x$  nanoparticles in 0.1 M  $\text{H}_2\text{SO}_4$  electrolyte was reported in a previous publication.<sup>25</sup> Based on these findings, it is certain that the  $\text{NbO}_x/\text{CB}$  nanoparticles can drive the ORR in both acidic and alkaline media.

Fig. 5(B) shows Nyquist plots of the N-doped  $\text{NbO}_x/\text{CB}$ ,  $\text{NbO}_x/\text{CB}$  (annealed in Ar), and as-deposited  $\text{NbO}_x/\text{CB}$  catalysts in the 0.1 M KOH solutions at an applied potential of 0.72 V<sub>RHE</sub>. The EIS measurements were performed to determine the effect of N-doping on the ORR activity of  $\text{NbO}_x/\text{CB}$ , namely, to evaluate the charge transfer behavior of the prepared catalysts during the ORR process. The fitting results of the Nyquist plots using an equivalent circuit model are summarized in Table S2 (ESI†). The electron transfer resistance,  $R_{\text{ct}}$ , at the interface between the catalyst and solution was significantly reduced after annealing treatments.  $R_{\text{ct}}$  was minimum in the N-doped  $\text{NbO}_x/\text{CB}$  catalyst, revealing that the annealing in  $\text{NH}_3$  efficiently enhanced the electroconductivity of the catalyst. The annealing in Ar was found to modify the surface of catalyst as shown in the XPS result in Fig. 2, indicating the removal of oxygen species such as  $\text{O}^{2-}$  in oxide and surface-adsorbed  $\text{OH}^-/\text{H}_2\text{O}$ . The loss of oxygen was accelerated in the reducing  $\text{NH}_3$  flow. Also, the small amount of nitrogen in the  $\text{NH}_3$

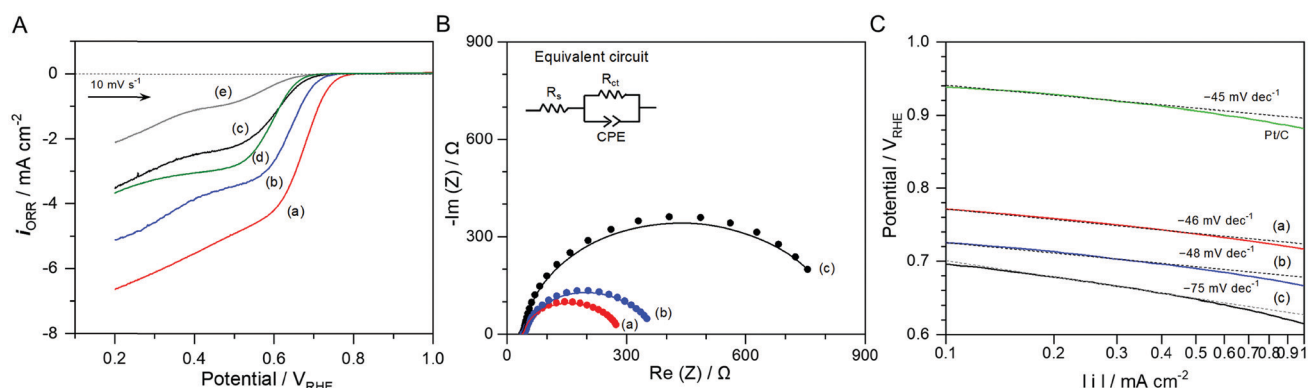


**Fig. 5** (A) LSVs for the ORR in  $\text{O}_2$ -purged 0.1 M KOH aqueous solutions using (a) the N-doped  $\text{NbO}_x/\text{CB}$  and (b)  $\text{NbO}_x/\text{CB}$  annealed in  $\text{NH}_3$  and Ar and at 873 K for 1 h, respectively, and (c) as-deposited  $\text{NbO}_x/\text{CB}$ , (d) CB, and (e) glassy carbon. (B) Nyquist plots of the prepared  $\text{NbO}_x/\text{CB}$  catalyst series. The EIS measurements were performed in the  $\text{O}_2$ -purged 0.1 M KOH aqueous solutions at an applied potential of 0.72 V<sub>RHE</sub>. The equivalent circuit model for the best-fits of Nyquist plots is shown in the inset of the figure. Fitting results are summarized in Table S2 (ESI†). (C) Tafel plots of the prepared  $\text{NbO}_x/\text{CB}$  catalyst series corresponding to the ORR curves shown in (A). The Tafel plot of the commercial 20 wt% Pt/CB powder was also compared in the same manner.



atmosphere was doped into the  $\text{NbO}_x$  nanoparticles. Typically, the doping of nitrogen in the group 4 or 5 metal oxides, as an insulator inherently, mainly enhanced the electroconductivity of the oxide itself, resulting in improved electrochemical activity for the ORR.<sup>22,40</sup> In this study, the modified surface of the  $\text{NbO}_x$  catalyst, originating from the annealing, largely promoted the electrocatalysis. Therefore, the largely enhanced ORR activity was attributed to more concentrated Nb and the doping of nitrogen in  $\text{NbO}_x$  nanoparticles.

Tafel plots of all the samples at low overpotentials against a thermodynamic potential of 1.23 V, obtained from Fig. 5(A), are shown in Fig. 5(C); the Tafel plot of 20 wt% Pt/CB was also compared. The Tafel slope for the as-deposited  $\text{NbO}_x$ /CB was approximately  $-75 \text{ mV dec}^{-1}$ . However, it became smaller after the annealing treatment in Ar and  $\text{NH}_3$  atmospheres, indicating that ORR kinetics was faster and the rate-determining step for the ORR was changed. These are in good agreement with the Nyquist results showing the annealing effect of the  $\text{NbO}_x$  catalyst. The Tafel slope was determined as  $-46 \text{ mV dec}^{-1}$  for the N-doped  $\text{NbO}_x$ /CB, which is similar to  $-45 \text{ mV dec}^{-1}$  for Pt/CB in this study. A Tafel slope of  $120 \text{ mV dec}^{-1}$  typically suggests that the one-electron transfer reaction is the rate-determining step for the ORR and the surface sites of the catalyst are stable under the measurement conditions. In acidic media, the surface of metallic Pt could be oxidized to  $\text{PtO}$  so that a smaller slope of *ca.*  $60 \text{ mV dec}^{-1}$  was observed for the ORR in the low overpotential range in previous reports.<sup>41,42</sup> The similar electrochemical behavior was also reported in alkaline media.<sup>43,44</sup> After the annealing, the concentration of surface oxygen on the catalyst was reduced, presumably leading to electroactive  $\text{NbO}_x$  surface sites for the ORR and thus the decrease in the Tafel slope at low overpotentials. A previous theoretical study on the various surface coverages such as  $\text{MOO}$ ,  $\text{MOO}^-$ , and  $\text{MOOH}$  ( $\text{M}$  = metal) showed different Tafel slopes during the ORR.<sup>43</sup> Thus, the small slope for the annealed  $\text{NbO}_x$ /CB nanoparticles might result from the variable surface states of the non-stoichiometric  $\text{NbO}_x$ , like a metallic Pt.

The RRDE measurement of N-doped  $\text{NbO}_x$ /CB nanoparticles was carried out during the ORR in  $\text{O}_2$ -saturated 0.1 M KOH electrolyte (Fig. S5, ESI†). The voltammogram was recorded at a sweep rate of  $5 \text{ mV s}^{-1}$ , although the ORR activity of the catalyst was nearly unchanged from that shown in Fig. 5(A) and scanned at  $10 \text{ mV s}^{-1}$ . The anodic current was observed on the Pt ring electrode, indicating that a  $\text{H}_2\text{O}_2$  byproduct was partly produced during the ORR *via* a two-electron transfer pathway. At a potential of  $0.5 \text{ V}_{\text{RHE}}$ , the  $\text{H}_2\text{O}_2$  yield originating from the ORR over the catalyst was estimated to be 32%, much lower than 67% in the ORR using bare CB particles. Moreover, the ring current began to be produced at  $0.68 \text{ V}_{\text{RHE}}$ , close to the onset potential of CB for the ORR. These results imply that the ORR *via* the two-electron transfer pathway was mainly catalyzed by the bare CB support. In addition, hydrodynamic voltammetry of N-doped  $\text{NbO}_x$ /CB nanoparticles was measured using a RDE at different revolution rates between 400 to 2500 rpm to establish the ORR kinetics (Fig. S6, ESI†). The ORR current at low potentials increased with increasing rotation rate, indicating that it was dominated by the diffusion-limiting current. The Koutecky-Levich plots for the nanoparticles exhibited a linear relationship between  $|i|^{-1}$  and  $\omega^{-1/2}$  and the slopes at the designated potentials were nearly close to four electron transfer. This indicates that the ORR process over the N-doped  $\text{NbO}_x$ /CB nanoparticles was governed by the four electron transfer pathway in the mass-transfer region.

Fig. 6(A) shows LSVs of N-doped  $\text{NbO}_x$ /CB,  $\text{NbO}_x$ /CB (annealed in Ar), as-deposited  $\text{NbO}_x$ /CB, CB (annealed in  $\text{NH}_3$ ), and glassy carbon for the OER in the  $\text{O}_2$ -purged 0.1 M KOH solution. The LSVs were recorded in a cathodic sweep direction to avoid the self-oxidation of catalysts as shown in Fig. 4(A). The OER activity of the as-deposited  $\text{NbO}_x$ /CB was significantly low, even far from the OER benchmark value of  $10 \text{ mA cm}^{-2}$  at an end potential of  $2.0 \text{ V}_{\text{RHE}}$ . It was also lower than that of CB. The lower activity was mainly attributed to the presence of excess oxygen species maintained after the electrodeposition. The excess oxygen covered on the surfaces of  $\text{NbO}_x$ /CB particles might suppress the electrocatalysis for the OER. The anodic current was enhanced

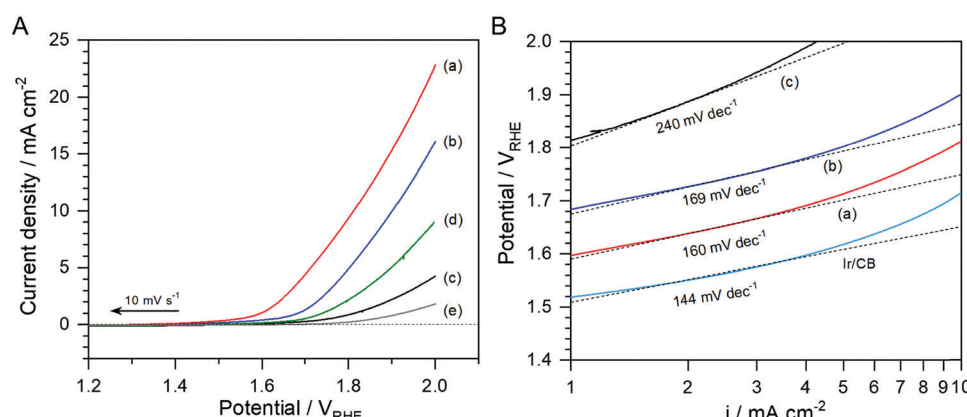


Fig. 6 (A) LSVs for the OER in  $\text{O}_2$ -purged 0.1 M KOH aqueous solutions using (a) the N-doped  $\text{NbO}_x$ /CB and (b)  $\text{NbO}_x$ /CB annealed in  $\text{NH}_3$  and Ar and at 873 K for 1 h, respectively, and (c) as-deposited  $\text{NbO}_x$ /CB, (d) CB, and (e) glassy carbon. (B) Tafel plots of the prepared  $\text{NbO}_x$ /CB catalyst series corresponding to the OER curves shown in (A). The Tafel plot of the commercial 20 wt% Ir/CB powder was also compared in the same manner.



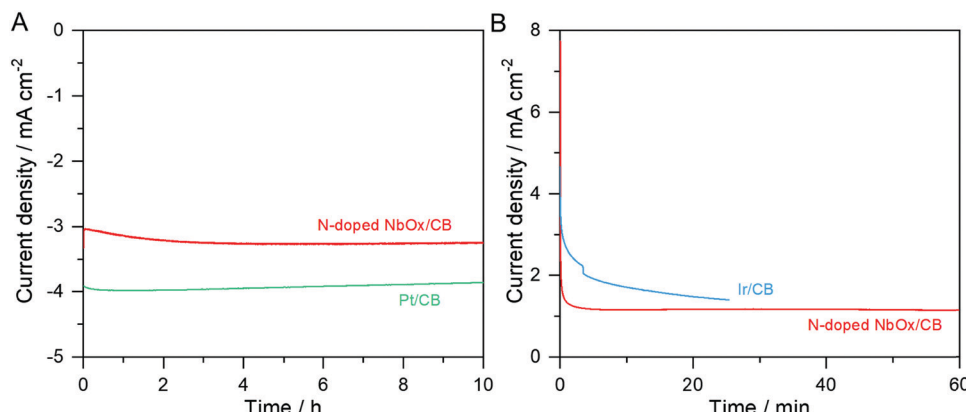


Fig. 7 (A) CA curves of the prepared N-doped NbO<sub>x</sub>/CB nanoparticles during the ORR applied at 0.65  $V_{\text{RHE}}$  for 10 h and (B) during the OER applied at 1.61  $V_{\text{RHE}}$  for 1 h, respectively, in O<sub>2</sub>-purged 0.1 M KOH aqueous solutions. For comparison, commercial 20 wt% Pt/CB and Ir/CB catalysts were also measured at 0.80  $V_{\text{RHE}}$  (for the ORR) and 1.61  $V_{\text{RHE}}$  (for the OER), respectively.

after the annealing in Ar, and it was remarkably increased by the annealing in NH<sub>3</sub>. The activity trend in the OER was similar to that in the ORR. The modified surface of the NbO<sub>x</sub> nanoparticles, *i.e.*, the removal of excess oxygen and the doping of nitrogen, led to the improvement in the electroconductivity of the catalysts and thus largely activated the catalysis for the OER as well as the ORR. In the Tafel plots, shown in Fig. 6(B), the slope of the N-doped NbO<sub>x</sub>/CB nanoparticles, indicating approximately 160 mV dec<sup>-1</sup>, was rather close to 120 mV dec<sup>-1</sup> than 60 mV dec<sup>-1</sup>. This reveals the N-doped NbO<sub>x</sub> during the OER was electrochemically stable at the oxidizing potentials. The nearly one-electron transfer reaction was the rate determining step during the OER process at low overpotentials over the prepared nanoparticles. The OER kinetics on the nanoparticles was slower than that of the commercial Ir/CB catalyst, judged by the Tafel slopes. However, it was clearly distinguishable from 240 mV dec<sup>-1</sup> for the as-deposited NbO<sub>x</sub>/CB. After the annealing, the significant decrease in the slope for the OER was consistent with that for the ORR. Therefore, the annealing in NH<sub>3</sub> enhanced both the ORR and OER kinetics, resulting from the surface modification of the NbO<sub>x</sub>/CB nanoparticles.

Fig. 7 shows CA curves of the N-doped NbO<sub>x</sub>/CB catalyst during the ORR and OER in the O<sub>2</sub>-purged 0.1 M KOH electrolytes. For comparison, the commercial 20 wt% Pt/CB and Ir/CB were also evaluated in the same manner. In Fig. 7(A), the ORR activity of the N-doped NbO<sub>x</sub>/CB nanoparticles applied at 0.65  $V_{\text{RHE}}$  was increased at the beginning point and then kept at a constant value of  $-3.3 \text{ mA cm}^{-2}$  for the 10 h reaction, while it was gradually decreased on the Pt/CB catalyst. It is remarkable that the nanoparticles were stable for long-term ORR in alkaline media. The Ta-based oxide nanoparticles were also durable for the ORR in an acidic electrolyte in previous results.<sup>28</sup> Therefore, we may conclude that the ORR is steadily catalyzed on the oxide nanoparticles, regardless of the pH level of the electrolyte. In addition, the long-term OER activity of the nanoparticles was measured at a benchmark potential of 1.81  $V_{\text{RHE}}$  for 10 mA cm<sup>-2</sup>. However, the O<sub>2</sub> evolution was very vigorous to an extent that the catalyst was detached from a

RDE and the catalytic stability could not be measured. The OER activity was thus evaluated at a potential of 1.61  $V_{\text{RHE}}$ , which was lower than the benchmark potential, for 1 h. As shown in Fig. 7(B), the anodic current was relatively stable as compared to that of the Ir/CB catalyst. Therefore, these results demonstrate that the catalytic activities over the N-doped NbO<sub>x</sub>/CB nanoparticles were stable in both the ORR and OER atmospheres.

## 4. Conclusions

In this study, for the first time, N-doped NbO<sub>x</sub>/CB nanoparticles were introduced as an active and stable bifunctional oxygen electrocatalyst in alkaline media. The NbO<sub>x</sub> nanoparticles of approximately 3 nm in size were successfully synthesized on the CB surfaces by potentiostatic electrodeposition in a non-aqueous solution and subsequent annealing treatment in a NH<sub>3</sub> flow. The annealing in the NH<sub>3</sub> significantly decreased the concentration of oxygen in the NbO<sub>x</sub> particles and doped additional nitrogen content. Also, the N-doped NbO<sub>x</sub> particles were made of Nb<sup>4+</sup> and Nb<sup>5+</sup> species, as confirmed by the XPS results. The employment of a CB support with a large surface area led to a large loading amount of 20 wt% NbO<sub>x</sub> particles and highly uniform distribution on the CB, increasing the number of reaction sites. Together, these properties remarkably enhanced the catalytic activities of the N-doped NbO<sub>x</sub>/CB nanoparticles for the ORR and OER in a 0.1 M KOH solution. The potential difference,  $\Delta E$ , indicating an index for the bifunctional oxygen electrocatalyst, was 1.13 V for the N-doped NbO<sub>x</sub>/CB particles. The bifunctional oxygen electrocatalysis was comparable to those of the commercial Pt/CB and Ir/CB. According to Koutecky-Levich plots, the ORR process over the N-doped NbO<sub>x</sub>/CB nanoparticles was governed by the four electron transfer pathway in the mass-transfer region. In addition, the current densities over the nanoparticles were stable in the ORR for 10 h at a potential of 0.65  $V_{\text{RHE}}$  and the OER for 1 h at a potential of 1.61  $V_{\text{RHE}}$ . These results demonstrate the N-doped



NbO<sub>x</sub>/CB nanoparticles as a novel bifunctional oxygen electrocatalyst that is active and stable for both the ORR and OER in alkaline media.

## Conflicts of interest

There are no conflicts to declare.

## Acknowledgements

This work was financially supported by the National Research Foundation of Korea (NRF) grant funded by the Korean government (MSIT) (No. 2020R1C1C1006373).

## References

- 1 M. Shao, Q. Chang, J. P. Dodelet and R. Chenitz, Recent Advances in Electrocatalysts for Oxygen Reduction Reaction, *Chem. Rev.*, 2016, **116**(6), 3594–3657.
- 2 Z.-F. Huang, J. Wang, Y. Peng, C.-Y. Jung, A. Fisher and X. Wang, Design of Efficient Bifunctional Oxygen Reduction/Evolution Electrocatalyst: Recent Advances and Perspectives, *Adv. Energy Mater.*, 2017, **7**(23), 1700544.
- 3 N. T. Suen, S. F. Hung, Q. Quan, N. Zhang, Y. J. Xu and H. M. Chen, Electrocatalysis for the oxygen evolution reaction: recent development and future perspectives, *Chem. Soc. Rev.*, 2017, **46**(2), 337–365.
- 4 Z. L. Wang, D. Xu, J. J. Xu and X. B. Zhang, Oxygen electrocatalysts in metal-air batteries: from aqueous to nonaqueous electrolytes, *Chem. Soc. Rev.*, 2014, **43**(22), 7746–7786.
- 5 X. Wu, C. Tang, Y. Cheng, X. Min, S. P. Jiang and S. Wang, Bifunctional Catalysts for Reversible Oxygen Evolution Reaction and Oxygen Reduction Reaction, *Chem. – Eur. J.*, 2020, **26**, 3906–3929.
- 6 X. Zhang, X. Xu, S. Yao, C. Hao, C. Pan, X. Xiang, Z. Q. Tian, P. K. Shen, Z. Shao and S. P. Jiang, Boosting Electrocatalytic Activity of Single Atom Catalysts Supported on Nitrogen-Doped Carbon through N Coordination Environment Engineering, *Small*, 2022, **18**(10), e2105329.
- 7 Z.-C. Yao, T. Tang, J.-S. Hu and L.-J. Wan, Recent Advances on Nonprecious-Metal-Based Bifunctional Oxygen Electrocatalysts for Zinc–Air Batteries, *Energy Fuels*, 2021, **35**(8), 6380–6401.
- 8 Y. Lee, J. Suntivich, K. J. May, E. E. Perry and Y. Shao-Horn, Synthesis and Activities of Rutile IrO<sub>2</sub> and RuO<sub>2</sub> Nanoparticles for Oxygen Evolution in Acid and Alkaline Solutions, *J. Phys. Chem. Lett.*, 2012, **3**(3), 399–404.
- 9 H. Y. Su, Y. Gorlin, I. C. Man, F. Calle-Vallejo, J. K. Norskov, T. F. Jaramillo and J. Rossmeisl, Identifying active surface phases for metal oxide electrocatalysts: a study of manganese oxide bi-functional catalysts for oxygen reduction and water oxidation catalysis, *Phys. Chem. Chem. Phys.*, 2012, **14**(40), 14010–14022.
- 10 Y. Gorlin and T. F. Jaramillo, A Bifunctional Nonprecious Metal Catalyst for Oxygen Reduction and Water Oxidation, *J. Am. Chem. Soc.*, 2010, **132**, 13612–13614.
- 11 K. Bradley, K. Giagloglou, B. E. Hayden, H. Jungius and C. Vian, Reversible perovskite electrocatalysts for oxygen reduction/oxygen evolution, *Chem. Sci.*, 2019, **10**(17), 4609–4617.
- 12 X. Xu, Y. Pan, Y. Zhong, C. Shi, D. Guan, L. Ge, Z. Hu, Y. Y. Chin, H. J. Lin, C. T. Chen, H. Wang, S. P. Jiang and Z. Shao, New Undisputed Evidence and Strategy for Enhanced Lattice-Oxygen Participation of Perovskite Electrocatalyst through Cation Deficiency Manipulation, *Adv. Sci.*, 2022, e2200530.
- 13 A. Restovic, E. Ríos, S. Barbato, J. Ortiz and J. L. Gautier, Oxygen reduction in alkaline medium at thin Mn<sub>x</sub>Co<sub>3-x</sub>O<sub>4</sub> (0 ≤ x ≤ 1) spinel films prepared by spray pyrolysis. Effect of oxide cation composition on the reaction kinetics, *J. Electroanal. Chem.*, 2002, **522**, 141–151.
- 14 A. J. Esswein, M. J. McMurdo, P. N. Ross, A. T. Bell and T. D. Tilley, Size-Dependent Activity of Co<sub>3</sub>O<sub>4</sub> Nanoparticle Anodes for Alkaline Water Electrolysis, *J. Phys. Chem. C*, 2009, **113**, 15068–15072.
- 15 E. Ríos, J.-L. Gautier, G. Poillerat and P. Chartier, Mixed valency spinel oxides of transition metals and electrocatalysis: case of the Mn<sub>x</sub>Co<sub>3-x</sub>O<sub>4</sub> system, *Electrochim. Acta*, 1998, **44**, 1491–1497.
- 16 H. M. Zhang, Y. Shimizu, Y. Teraoka, N. Miura and N. Yamazoe, Oxygen sorption and catalytic properties of La<sub>1-x</sub>Sr<sub>x</sub>Co<sub>1-y</sub>FeyO<sub>3</sub> perovskite-type oxides, *J. Catal.*, 1990, **121**, 432–440.
- 17 H. Tanaka and M. Misono, Advances in designing perovskite catalysts, *Curr. Opin. Solid State Mater. Sci.*, 2001, **5**, 381–387.
- 18 A. Kahoul, A. Hammouche, G. Poillerat and R. W.-D. Doncker, Electrocatalytic activity and stability of La<sub>1-x</sub>Ca<sub>x</sub>-CoO<sub>3</sub> perovskite-type oxides in alkaline medium, *Catal. Today*, 2004, **89**(3), 287–291.
- 19 N.-L. Wu, W.-R. Liu and S.-J. Su, Effect of oxygenation on electrocatalysis of La<sub>0.6</sub>Ca<sub>0.4</sub>CoO<sub>3-x</sub> in bifunctional air electrode, *Electrochim. Acta*, 2003, **48**(11), 1567–1571.
- 20 S. Malkhandi, B. Yang, A. K. Manohar, A. Manivannan, G. K. Prakash and S. R. Narayanan, Electrocatalytic Properties of Nanocrystalline Calcium-Doped Lanthanum Cobalt Oxide for Bifunctional Oxygen Electrodes, *J. Phys. Chem. Lett.*, 2012, **3**(8), 967–972.
- 21 R. Ohnishi, K. Takanabe, M. Katayama, J. Kubota and K. Domen, Nano-nitride Cathode Catalysts of Ti, Ta, and Nb for Polymer Electrolyte Fuel Cells: Temperature-Programmed Desorption Investigation of Molecularly Adsorbed Oxygen at Low Temperature, *J. Phys. Chem. C*, 2012, **117**(1), 496–502.
- 22 A. Ishihara, K. Lee, S. Doi, S. Mitsushima, N. Kamiya, M. Hara, K. Domen, K. Fukuda and K.-I. Ota, Tantalum Oxynitride for a Novel Cathode of PEFC, *Electrochim. Solid-State Lett.*, 2005, **8**(4), A201.
- 23 Y. Ohgi, A. Ishihara, K. Matsuzawa, S. Mitsushima and K. Ota, Zirconium Oxide-Based Compound as New Cathode Without Platinum Group Metals for PEFC, *J. Electrochem. Soc.*, 2010, **157**(6), B885.



24 J. Seo, D. Cha, K. Takanabe, J. Kubota and K. Domen, Particle size dependence on oxygen reduction reaction activity of electrodeposited  $TaO(x)$  catalysts in acidic media, *Phys. Chem. Chem. Phys.*, 2014, **16**(3), 895–898.

25 J. Seo, D. Cha, K. Takanabe, J. Kubota and K. Domen, Electrodeposited Ultrafine  $NbO_x$ ,  $ZrO_x$ , and  $TaO_x$  Nanoparticles on Carbon Black Supports for Oxygen Reduction Electrocatalysts in Acidic Media, *ACS Catal.*, 2013, **3**(9), 2181–2189.

26 X. Zhang, J. Guo, P. Guan, C. Liu, H. Huang, F. Xue, X. Dong, S. J. Pennycook and M. F. Chisholm, Catalytically active single-atom niobium in graphitic layers, *Nat. Commun.*, 2013, **4**, 1924.

27 J. C. Ruiz-Cornejo, D. Sebastián, M. V. Martínez-Huerta and M. J. Lázaro, Tantalum-based electrocatalysts prepared by a microemulsion method for the oxygen reduction and evolution reactions, *Electrochim. Acta*, 2019, **317**, 261–271.

28 J. Seo, D. H. Anjum, K. Takanabe, J. Kubota and K. Domen, Electrodeposited Ultrafine  $TaO_x/CB$  Catalysts for PEFC Cathode Application: Their Oxygen Reduction Reaction Kinetics, *Electrochim. Acta*, 2014, **149**, 76–85.

29 R. Neffati and J. M.-C. Brokken-Zijp, Structure and porosity of conductive carbon blacks, *Mater. Chem. Phys.*, 2021, **260**, 124177.

30 H. D. Asfaw, C.-W. Tai, L. Nyholm and K. Edström, Overstoichiometric  $NbO_2$  nanoparticles for a high energy and power density lithium microbattery, *ChemNanoMat*, 2017, **3**, 646–655.

31 M. K. Hota, M. K. Bera, S. Verma and C. K. Maiti, Studies on switching mechanisms in Pd-nanodot embedded  $Nb_2O_5$  memristors using scanning tunneling microscopy, *Thin Solid Films*, 2012, **520**(21), 6648–6652.

32 M. Ziolek and I. Nowak, Characterization techniques employed in the study of niobium and tantalum-containing materials, *Catal. Today*, 2003, **78**(1-4), 543–553.

33 S. Martínez-Méndez, Y. Henríquez, O. Domínguez, L. D'Ornelas and H. Krentzien, Catalytic properties of silica supported titanium, vanadium and niobium oxide nanoparticles towards the oxidation of saturated and unsaturated hydrocarbons, *J. Mol. Catal. A: Chem.*, 2006, **252**(1-2), 226–234.

34 S. Ramaraj and J. Seo, Intensive-visible-light-responsive  $ANbO_2N$  ( $A = Sr, Ba$ ) synthesized from layered perovskite  $A_3Nb_4O_{15}$  for enhanced photoelectrochemical water splitting, *J. Energy Chem.*, 2022, **68**, 529–537.

35 T. T.-T. Tran, S. Kim and J. Seo, Size dependence of perovskite-type  $BaNbO_2N$  particles on sunlight-driven photoelectrochemical water splitting, *J. Catal.*, 2022, **406**, 157–164.

36 F. J. Sotomayor, K. A. Cychosz and M. Thommes, Characterization of Micro/Mesoporous Materials by Physisorption: Concepts and Case Studies, *Acc. Mater. Surf. Res.*, 2018, **3**(2), 34–50.

37 J. S. Lee, G. S. Park, H. I. Lee, S. T. Kim, R. Cao, M. Liu and J. Cho, Ketjenblack carbon supported amorphous manganese oxides nanowires as highly efficient electrocatalyst for oxygen reduction reaction in alkaline solutions, *Nano Lett.*, 2011, **11**(12), 5362–5366.

38 J.-W. Park and J. Seo, Ultrafine  $TaO_x/CB$  Oxygen Reduction Electrocatalyst Operating in Both Acidic and Alkaline Media, *Catalysts*, 2021, **12**(1), 35.

39 J. Seo, L. Zhao, D. Cha, K. Takanabe, M. Katayama, J. Kubota and K. Domen, Highly Dispersed  $TaO_x$  Nanoparticles Prepared by Electrodeposition as Oxygen Reduction Electrocatalysts for Polymer Electrolyte Fuel Cells, *J. Phys. Chem. C*, 2013, **117**(22), 11635–11646.

40 J. Chen, K. Takanabe, R. Ohnishi, D. Lu, S. Okada, H. Hatasawa, H. Morioka, M. Antonietti, J. Kubota and K. Domen, Nano-sized  $TiN$  on carbon black as an efficient electrocatalyst for the oxygen reduction reaction prepared using an mpg-C<sub>3</sub>N<sub>4</sub> template, *Chem. Commun.*, 2010, **46**(40), 7492–7494.

41 U. A. Paulus, T. J. Schmidt, H. A. Gasteiger and R. J. Behm, Oxygen reduction on a high-surface area Pt/Vulcan carbon catalyst a thin-film rotating ring-disk electrode study, *J. Electroanal. Chem.*, 2001, **495**, 134–145.

42 J. Perez, E. R. Gonzalez and E. A. Ticianelli, Oxygen electrocatalysis on thin porous coating rotating platinum electrodes, *Electrochim. Acta*, 1998, **44**, 1329–1339.

43 T. Shinagawa, A. T. Garcia-Esparza and K. Takanabe, Insight on Tafel slopes from a microkinetic analysis of aqueous electrocatalysis for energy conversion, *Sci. Rep.*, 2015, **5**, 13801.

44 L. Genies, R. Faure and R. Durand, Electrochemical reduction of oxygen on platinum nanoparticles in alkaline media, *Electrochim. Acta*, 1998, **44**, 1317–1327.

